

Status of Cooled and Uncooled Infrared Detectors at SCD, Israel

Philip Klipstein*, Udi Mizrahi, Rami Fraenkel, and Itay Shtrichman

Semi Conductor Devices, Haifa 31021, Israel

**E-Mail: philip_k@scd.co.il*

ABSTRACT

For the highest end mid-wave-infrared applications, SCD, France offers a family of cryogenically cooled detectors with background limited performance (BLIP). The matured InSb planar technology is implemented in a variety of focal plane arrays, from a 320 x 256 format with a 30 μm pitch to a 1280 x 1024 format with a 15 μm pitch, all of which are operated at 77K. A major challenge is to reduce the cooling requirements. Then substantial reductions in size, weight, and power (SWaP) can be achieved by using a smaller cooler and Dewar assembly. SCD's new epi-InSb detectors, grown by molecular beam epitaxy, have a BLIP temperature of ~ 100 K at F/3. This enhanced operating temperature reduces the required cooling power by ~ 20 % compared with the conventional 77 K operation. For a very high operating temperature, we have developed the new XBn-InAsSb detector with a 4.2 μm cut-off wavelength. This detector exhibits a BLIP temperature of ~ 160 K at F/3 and a reduction in cooling power of ~ 60 %. These HOT detectors enable an improved range of solutions, including faster cool-down time and mission readiness, longer mission times, and higher cooler reliability. We can also exploit their reduced dark current to obtain an enhanced signal to noise ratio at lower operating temperatures.

The well-established 25 μm pitch family of uncooled μ -Bolometer detectors has two basic formats, 384 x 288 and 640 x 480, and several sensitivity grades. The very high sensitivity 25 μm pitch detector has been demonstrated at F/2.4 for mid-range systems. The wide-band detector is optimized for both the long-wave-infrared and mid-wave-infrared spectral bands. Recently we developed the new 17 μm pitch family of detectors. The 640 x 480 format is a leading candidate for applications such as thermal weapon sights, driver vision enhancers and other mid-range IR systems. The 17 μm family is currently being expanded with the high sensitivity grade and with the addition of two new formats: the compact 384 x 288 for low SWaP applications, and the large 1024 x 768 format for applications requiring high resolution and a wide field of view.

Keywords: Infrared, photon detector, focal plane array, micro-bolometer

NOMENCLATURE

T	Temperature
I	Current
I_0	Dark current prefactor
ΔE	Activation Energy
λ	Wavelength
AL	Active layer
ARC	Anti reflection coating
BrL	Barrier layer
BLIP	Background limited performance
CL	Contact layer
DVE	Driver vision enhancer
FOV	Field of view
FPA	Focal plane array
G-R	Generation-recombination
HH	Hand held
HOT	High operating temperature
HS	High sensitivity
IDCA	Integrated dewar cooler assemblies
IFOV	Instantaneous field of view
LWIR	Long-wave-infrared
MBE	Molecular beam epitaxy
MCT	Mercury Cadmium Telluride
MTF	Modulation transfer function

MWIR	Mid-wave-infrared
NETD	Noise equivalent temperature difference
NUC	Non uniformity correction
QE	Quantum efficiency
QVGA	Quarter video graphics array (Format)
ROIC	Read out integrated circuit
RNU	Residual non uniformity
SNR	Signal to noise ratio
SWaP	Size, weight and power
TWS	Thermal weapons sight
TDI	Time delay integration
VGA	Video graphics array (Format)
VHS	Very high sensitivity
VLSI	Very large scale integration
WB	Wide band
XGA	Extended graphics array (Format)

1. INTRODUCTION

In this paper we present a short review of some of the recent developments in infrared (IR) focal plane array (FPA) technology at SCD, Israel. This technology can be divided into two broad classes which are based on essentially different physical principles, materials and processes. The first class

constitutes arrays of photovoltaic devices made from the $\text{InAs}_{1-x}\text{Sb}_x$ family of narrow bandgap semiconductors. Each device is bonded with an indium pillar to a pixel of a silicon read out integrated circuit (ROIC), fabricated by standard silicon VLSI methods. The whole assembly is cooled with a miniature Stirling or Joule-Thompson cooler in order to reduce the dark current to a level significantly below the photocurrent signal produced when light is absorbed. We have recently developed and patented a new type of photovoltaic device based on InAsSb/AlSbAs hetero-structures, which we have called an XB_n device. This technology can be said to supercede technologies based on homostructure photodiodes, and it has led to a substantial reduction in the FPA cooling requirement.

The FPA cooling requirement is entirely eliminated in the second class of detector technology. This technology uses a silicon micro-bolometer in each pixel with a weak thermal connection to the rest of the silicon ROIC. Small temperature changes induced by the absorption of infrared radiation lead to significant variations in the resistance of a Vanadium oxide resistor evaporated on the bolometer surface. The device is most sensitive in the long wave infrared (LWIR) spectral region (8-12 μm) although we shall discuss devices with a significant mid wave infrared (MWIR) response (3-5 μm), also. All of the cooled detectors that we shall discuss, both photodiode and XB_n, operate in the MWIR.

2. COOLED INASSB BASED DETECTORS

2.1 Diodes and Bariodes

The MWIR ‘window’ in the atmosphere is important for thermal sensing because it spans optical wavelengths from 3 μm to 5 μm where all room temperature objects emit significant quantities of electromagnetic radiation. High performance photodiode FPA detectors operating in the MWIR are usually made from the semiconductors Mercury Cadmium Telluride (MCT) or Indium Antimonide (*InSb*). One of the limiting factors in detector performance is the ‘dark current’ that arises from thermal excitation of charge carriers across the semiconductor bandgap. In the ‘diffusion limit’ this dark current is from minority carriers excited in the photon absorbing active layer which diffuse towards the collecting contact. A diffusion limited current can be achieved in the best MCT FPAs, which are grown on expensive Cadmium Zinc Telluride substrates¹. In contrast, even the best *InSb* FPAs are generation-recombination (G-R) limited². In this limit, Shockley-Read-Hall traps^{3,4}, created by imperfections in the semiconductor crystal lattice, provide energy states that lie in the semiconductor bandgap. These act as ‘stepping stones’ for electrons and holes to pass through when they are thermally excited. In the depletion region of the diode p-n junction, a built-in electric field exists which separates the electrons and holes before they can recombine. This provides a powerful driving force for the dark current. The dark current in *InSb* FPAs is therefore significantly higher than in MCT FPAs.

Both *InSb* and MCT detectors must be cooled cryogenically, typically with a miniature Joule Thomson or Stirling cycle refrigerator. The higher dark current in *InSb* is usually suppressed by operating the FPA at a temperature some tens of degrees Kelvin colder than the equivalent diffusion

limited MCT device. This apparent disadvantage is offset by the higher uniformity and pixel operability, together with the significantly lower cost per pixel of *InSb*, making it the current favourite for large scale arrays⁵.

At SCD we have adopted two approaches for reducing the dark current in *InSb* like FPAs, in order to close the gap with MCT while maintaining all of the advantages of *InSb*, including scalability to large areas at affordable cost. The first approach involves reducing the concentration of G-R centres at the p-n junction of our *InSb* diodes, while the second uses a new patented $\text{InAs}_{1-x}\text{Sb}_x$ n-type ‘bariodes’ technology to eliminate the G-R current entirely^{6,7}. Bariodes (‘Barrier-diodes’) can provide the same low diffusion limited dark current as MCT photodiodes with the same active layer bandgap. However, they utilize III-V semiconductor materials and also offer processing advantages.

The new n-type bariode detector⁸, also known as an XB_n detector, has a cut-off wavelength of approximately 4.1 μm and is based on a heterostructure design that can be grown with high quality on commercially available substrates. The XB_n detector contains an n- or p-type contact layer made from $\text{InAs}_{0.91}\text{Sb}_{0.09}$ or GaSb (X), a barrier layer made from n-type $\text{AlSb}_{0.91}\text{As}_{0.09}$ (B_n), and an active layer made from n-type $\text{InAs}_{0.91}\text{Sb}_{0.09}$ (n). These compositions are all closely lattice matched to GaSb, which can be used as the substrate. Figure 1 shows a schematic band diagram for an nB_nn device (X = n-type $\text{InAs}_{0.91}\text{Sb}_{0.09}$) at operating bias, where no depletion exists in the active layer. Note that all members of the n-type bariode family contain the same n-type barrier and active layer unit (‘B_nn’). The members of the polarity inverted p-type bariode family all contain the same p-type barrier and active layer unit (‘B_pp’). The latter can be realized using a Type II Superlattice as the active layer and are discussed elsewhere⁹. In both cases the barrier blocks the flow of majority carriers, while minority carriers have a clear path through the structure.

Both of our new technologies involve MBE growth. In the case of *InSb* diodes, a high quality homostructure is grown on an *InSb* substrate and diodes are isolated by etching a mesa structure through the p-n junction. Because implantation

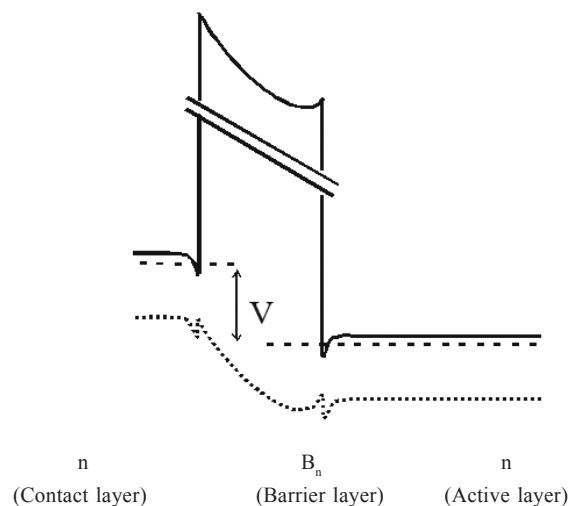


Figure 1. Schematic band diagram of an nB_nn bariode at operating bias.

damage is avoided, they have a much lower concentration of G-R centres than our standard planar p - n junctions. The dark current is thus reduced according to the ratio of concentrations of G-R centres in the standard and MBE grown structures. This is shown schematically by the grey curves in Fig. 2, which display typical plots of the logarithm of the dark current vs. the reciprocal of the temperature. The steeper part of each curve is diffusion limited dark current and the less steep part is G-R limited. For a given dark current the operating temperature is increased, according to the grey horizontal arrow drawn in Fig. 2. Note that for epi-InSb the cut-off wavelength is $5.4 \mu\text{m}$, as for standard planar InSb.

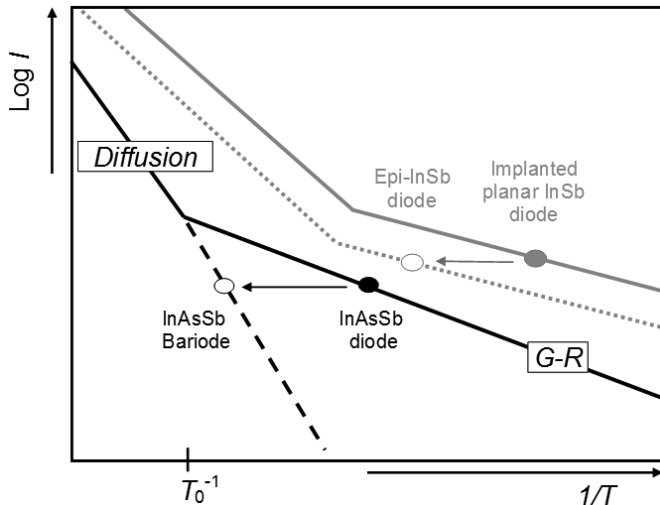


Figure 2. Schematic Arrhenius plot of temperature dependence of the dark current in InSb diodes and $\text{InAs}_{0.91}\text{Sb}_{0.09}$ diodes and bariorodes grown by MBE. The diffusion and G-R limited portions of the $\text{InAs}_{0.91}\text{Sb}_{0.09}$ curves are labeled.

In an XB_n (or XB_p) detector, the bulk G-R current is totally suppressed by excluding the depletion electric field from the narrow bandgap photon absorbing active layer material (as shown in Fig. 1). The black lines in Fig. 2 show a comparison between an ideal standard $\text{InAs}_{0.91}\text{Sb}_{0.09}$ diode and an $\text{InAs}_{0.91}\text{Sb}_{0.09}$ n-type bariorode. Note that the crossover temperature T_0 between diffusion and G-R limited dark current is higher in $\text{InAs}_{0.91}\text{Sb}_{0.09}$ because it has a larger bandgap than InSb⁸. Since the operating point in the bariorode is only limited by diffusion, the operating temperature is increased relative to the diode, according to the horizontal black arrow drawn in Fig. 2. In this way we have achieved $\text{InAs}_{0.91}\text{Sb}_{0.09}$ bariorode detector operation at F/3 with background limited performance (BLIP) at temperatures exceeding 160 K, more than doubling the traditional InSb operating temperature.

Note that in both epi-InSb and XB_n $\text{InAs}_{0.91}\text{Sb}_{0.09}$, the devices can be operated at a lower temperature, more typical of planar InSb, in which case they both have an extremely small dark current. This is good for applications where the incident photon intensity is very low and the dark current would otherwise limit the SNR.

The reductions in dark current and the corresponding increases in operating temperature that can be achieved with

our MBE based epi-InSb diode and $\text{InAs}_{0.91}\text{Sb}_{0.09}$ bariorode technologies have important consequences on the size (S), weight (W) and required cooling power (P), or SWaP, of the integrated Dewar cooler assemblies (IDCAs) made with these FPA detectors. Table 1 shows values of the IDCA parameters related to closed cycle Stirling cooler performance at an ambient temperature of 23°C , for planar and epi-InSb diodes and $\text{InAs}_{0.91}\text{Sb}_{0.09}$ bariorodes. The similar cool down times for planar and epi-InSb reflect the trade-off between a larger cooler for a smaller operating temperature and vice versa. The successive increases in operating temperature on going from planar to epi-InSb diodes to $\text{InAs}_{0.91}\text{Sb}_{0.09}$ bariorodes deliver a considerable reduction in required cooling power. Size and weight are also reduced substantially (for example using the Ricor K562S cooler instead of K561), leading to an IDCA with a much reduced SWaP. Table 1 also shows that the cooler (and IDCA) reliability increases significantly as the operating temperature is raised.

Table 1. Compares some of the key IDCA parameters related to closed cycle Stirling cooler performance, for the standard planar and MBE based FPAs.

Parameter	Planar InSb	epi-InSb	$\text{InAs}_{0.91}\text{Sb}_{0.09}$ Bariorode
Ricor Cooler type (max heat load)	K561 (0.3W)	K562S (0.25W)	K562S (0.25W)
Weight	290 g	185 g	185 g
FPA Operating temperature	77 K	95 K	150 K
Cooling power	5 W	4 W	2 W
Cool down time	6 min	6 min	3 min
Reliability (MTTF)	5,000 h	5,800 h	>10,000 h

2.2 System Performance vs Cut-off Wavelength

When going to shorter MWIR cut-off wavelengths, the photon flux is reduced dramatically. Combined with the small pixel area, it would seem at first sight that a higher noise equivalent temperature difference (NETD) would result and the radiometric performance would be degraded significantly at the system level. However, the short cut-off wavelength turns out to have major advantages for applications related to long range observation. In standard atmospheric conditions, the optical transmission at wavelengths shorter than that of the CO_2 absorption line ($4.2 - 4.4 \mu\text{m}$) is much higher than the transmission at longer wavelengths. For example, in the ninth line of Table 2 a comparison is made between 2 detectors, one having a cut-off wavelength of $4.9 \mu\text{m}$ and a calculated NETD of 23 mK and the other with a cut-off wavelength of $4.1 \mu\text{m}$ and a calculated NETD of 63 mK. Due to the better atmospheric transmission at shorter cut-off wavelengths, the detection ranges of both detectors are similar. It should be noted that shorter wavelengths result in smaller diffraction effects, and the resulting improvement in spatial resolution also contributes to an increased detection range.

In the rest of this section, simulations of system performance are presented for two spectral windows, $3.4 \mu\text{m} - 4.1 \mu\text{m}$ and

3.4 μm – 4.9 μm , corresponding to the sensitivity ranges for XB_n and InSb detectors, respectively (for InSb, an external cold filter is used to cut-off the radiation at 4.9 μm). In the simulations, the detector dark current in the first window is that typical of an XB_n detector operating at 150 K, while in the second it is typical of an epi-InSb detector operating at 95 K. At low environmental temperatures (-20 $^\circ\text{C}$), however, the XB_n temperature is lowered to 140 K, in order to reduce the dark current further and improve the signal to noise ratio (SNR). The dark current behaviour of the two detector families will be discussed in detail in the two sections following this one.

For the system level performance, we first calculate the SNR as a function of the cut-off wavelength. This calculation takes atmospheric absorption into account, which reduces the signal especially for long target distances, and also atmospheric emission and the emission of the optics, which both contribute to the noise. In the following calculations, two different systems are considered. One is a hand held system with F/4, 200 mm optics, operated at 60 Hz and an integration time of 16 msec. The other system is for long range observation applications with F/5.5, 900 mm optics. This system works at a slower frame rate of 25 Hz with an integration time of 40 msec. In Fig. 3, the SNR is presented versus cut-off wavelength (a) for the hand held detector system looking at scenery 5 km away, and (b) for the long range observation system looking at scenery 15 km away. For each system, three environmental temperatures are considered, -20 $^\circ\text{C}$, 0 $^\circ\text{C}$, and 27 $^\circ\text{C}$, and a temperature contrast

of 1 $^\circ\text{C}$ is assumed in the landscape. In the simulation the same temperature is used for the landscape, the atmosphere and the optics. U.S. Standard atmospheric absorption spectra are used for hot scenery at 27 $^\circ\text{C}$ and a sub-arctic atmosphere is used for cold environmental temperatures of 0 $^\circ\text{C}$ and -20 $^\circ\text{C}$.

It is possible to see from Fig. 3, that there is an improvement in the SNR at first, as the cut-off wavelength increases, but then the SNR decreases near the CO_2 absorption line, due to the combined effects of stronger absorption and stray light from the atmosphere that increases the noise without contributing to the signal. As the cut-off wavelength is increased further, the SNR starts to increase again. At a high environmental temperature, it is apparent from Fig. 3, that the SNR in the 3.4 μm – 4.1 μm window is better than SNR in the full MWIR window. At lower scene temperatures however (0 $^\circ\text{C}$ and -20 $^\circ\text{C}$), the effect of the absorption of the atmosphere above the CO_2 line improves and total flux also plays a dominant roll, so the resulting SNR is higher in the full MWIR window. Nevertheless, it is clear that the SNR in the 3.4 μm – 4.1 μm band is greater than 4 in all cases, which is sufficient to allow a good quality image even in low temperature conditions. We believe that SNR=2 is the threshold for getting a landscape image in the system.

In Table 2, the detection and identification ranges at 90 % probability are compared for two detectors in the two spectral windows (3.4 μm - 4.1 μm and 3.4 μm - 4.9 μm). The comparison is made for the two systems mentioned above and for two standard targets: a NATO panel of size 2.3 m \times

Table 2. A comparison between the detection and identification ranges at 90 % probability for two detectors (short and long range) in two spectral windows (3.4 μm - 4.1 μm and 3.4 μm - 4.9 μm).

System – target	3.4 μm - 4.1 μm			3.4 μm - 4.9 μm		
	Detector NETD (mK)	Detection (90%) (km)	Identification (90%) (km)	Detector NETD (mK)	Detection (90%) (km)	Identification (90%) (km)
27 $^\circ\text{C}$						
1. Long range – NATO	26	27.8	6.7	19	23	6.4
2. Hand held – NATO	29	10.2	1.9	18	9.3	1.9
3. Long range – Human	26	15.6	2.8	19	15.1	2.8
4. Hand held – Human	29	4.6	0.8	18	4.5	0.8
0 $^\circ\text{C}$						
5. Long range – NATO	40	34	6.7	17	32.3	6.8
6. Hand held – NATO	45	10.5	1.8	18	10.9	1.9
7. Long range – Human	40	15.9	2.7	17	15.7	2.8
8. Hand held – Human	45	4.5	0.8	18	4.6	0.8
-20 $^\circ\text{C}$						
9. Long range – NATO	63	31.4	6.5	23	31	6.6
10. Hand held – NATO	74	9.9	1.7	26	10.2	1.9
11. Long range – Human	63	15.6	2.7	23	15.5	2.8
12. Hand held – Human	74	4.3	0.7	26	4.6	0.8

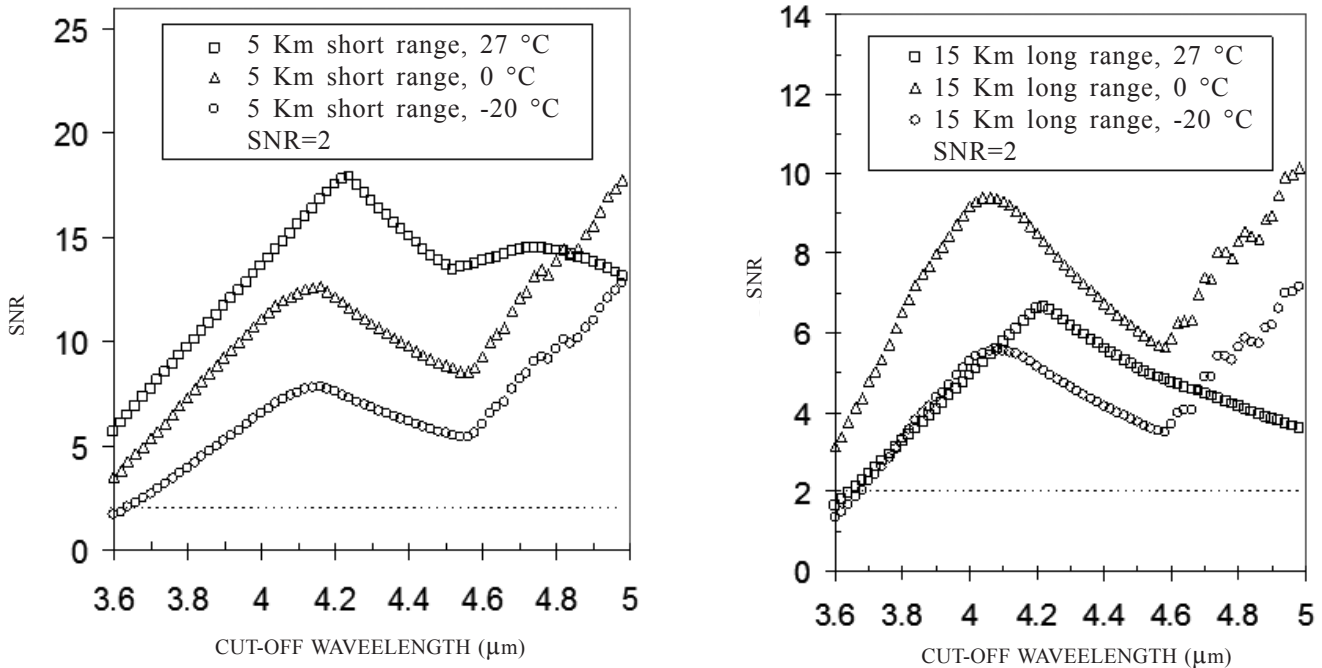


Figure 3. SNR versus cutoff for (a) a short range hand held system looking at scenery 5 km away and (b) a long range observation system looking at scenery 15 km away. For each system, 3 environmental temperatures are tested (-20 °C, 0 °C and 27 °C) where a temperature contrast of 1 °C in the landscape is assumed. In each plot, the dashed line indicates SNR=2, which is taken to be the threshold for a meaningful image.

2.3 m and a human target 1.5 m × 0.5 m, with temperature differences relative to their surroundings of 1.25 °C and 5 °C, respectively. The same environmental temperature range is considered as above (-20 °C, 0 °C, and 27 °C). It is apparent from Table 2, that in most scenarios both spectral bands have similar performance, except for the high temperature and long range application, where the spectral band of 3.4 μm - 4.1 μm has an advantage due to relatively high atmospheric absorption above the CO₂ line in a standard atmosphere.

2.3 Performance of Epi-InSb Diode FPA

The temperature dependence of the dark current in planar implanted InSb and Epi-InSb FPAs with a 15 μm pitch is compared in Fig. 4. The Epi-InSb FPA was fabricated by mesa etching an InSb epitaxial *p-n* structure grown on a 3' InSb substrate in a Veeco Gen 200 MBE machine. Both the planar and epi-InSb FPAs were bonded to SCDs Pelican ROIC (640 × 512, 15 μm pitch). For ease of comparison, the dark current has been normalized to that at the epi-InSb FPA operating temperature, *T* = 95 K (1000/*T* = 10.53). The lines through the points are fits to the data based on the G-R formula: $I = I_0 T^{3/2} \exp(-\Delta E/kT)$ where *k* = Boltzman's constant. In both cases, Δ*E* = 0.12 eV, which corresponds to approximately half the bandgap of InSb at low temperatures, exactly as expected for G-R limited behaviour¹⁰. The prefactors, *I*₀, are in the ratio 17.3, which represents the factor by which the dark current has been decreased by going to the MBE based technology. Note that the same dark current is achieved at 80 K in planar InSb and 95 K in epi-InSb.

Since the quantum efficiency (QE) is comparable (> 80%) for both technologies, the reduction of the dark current in epi-InSb allows the FPA operating temperature to be increased to 95

K with no loss of performance. The equivalence of performance is demonstrated in the next two figures, which compare the NETD distributions and the stability of the residual non-uniformity (RNU) to temperature drift (so called V-curves), respectively, for Pelican planar and epi-InSb FPAs. In Fig. 5, the NETD distributions are shown for planar InSb at 80 K, and epi-InSb at 95 K, measured in front of a 45 °C black body with an F/4.1 aperture and a 60 % well fill. They are virtually identical. In Fig. 6, the V-curve for epi-InSb at 95 K is similar to that of planar InSb at 80 K. The V-curve is a plot of the RNU

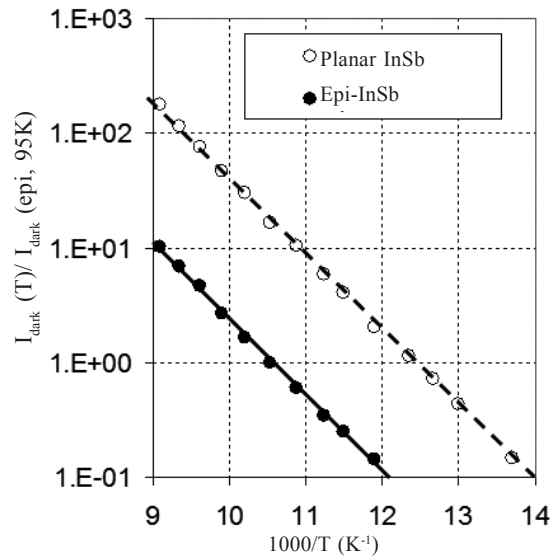


Figure 4. Temperature dependence of the mean dark current of Pelican FPAs (15 μm pitch), with planar (open points) and epi-InSb (solid points) diodes.

(at a well fill of 45 %) as the FPA temperature is varied from its calibration temperature. The calibration temperature is the temperature at which the minimum of the V-curve is located. The calibration was performed using a standard two point non uniformity correction¹¹, at well fill values of 30 % and 60 %, respectively. The V-curve is a measure of the stability of the FPA image quality with respect to temperature drift, where a wider curve corresponds to a greater stability. Epi-InSb at 95 K has a width of 7 K at RNU=0.1% and is actually more stable than planar InSb at 80 K, whose width is 4K. At 80 K the V-curve for epi-InSb is much wider than that for planar InSb, indicating the robustness of its RNU to temperature drift.

In Fig. 7 we show the temperature dependence of the NETD at F/4.1, and the pixel operability, in an epi-InSb Pelican FPA. It may be seen that the NETD hardly changes over a range of temperature up to about 100 K. Similarly, the number of defects, determined by SCD's standard production line criteria, essentially does not change in this temperature range. The pixel operability remains above 99.8 % up to 100 K. This shows that the epi-InSb Pelican detector has a useful operating range up to, and even beyond, 100 K.

An important issue in FPA image quality is pixel cross talk. This is the fraction of the light signal falling on a given pixel that is detected by one of its neighbours. It is most conveniently quantified by the Modulation Transfer Function (MTF). The MTF is the amplitude of a spatially periodic signal detected by the FPA as a function of the signal's spatial frequency. Details of the method of its measurement are given in Shtrichman¹², *et al.* In Fig. 8, MTF curves are compared for both planar and epi-InSb FPAs with three different pitches: 30 μm , 20 μm , and 15 μm , corresponding to SCDs Blue Fairy, Sebastian and Pelican ROICs, respectively. The epi-InSb MTF curves are wider than the corresponding curves for planar InSb for the two largest pitches, and are essentially identical for the smallest pitch. Together Figs. 5-8 demonstrate that the higher

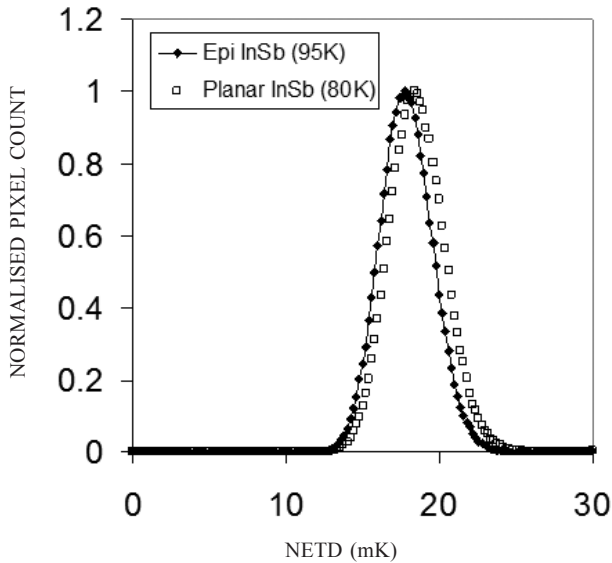


Figure 5. Comparison of the NETD distributions in Pelican FPAs, with implanted planar InSb diodes at 80 K and epi-InSb diodes at 95 K. The black body temperature was 45 °C and the measurement was performed with an aperture of F/4.1.

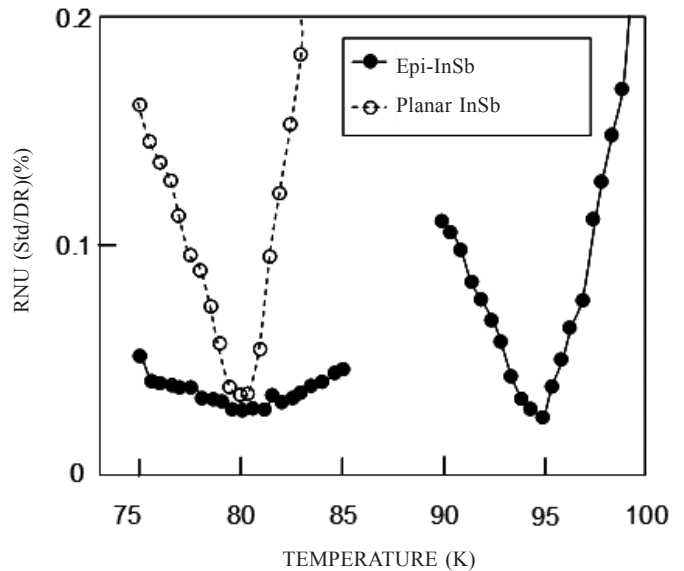


Figure 6. V-curves for implanted planar InSb (open) and epi-InSb (solid) Pelican FPAs, calibrated by a standard 2 point correction at either 80 K or 95 K.

operating temperature in epi-InSb has been achieved without any degradation of the image quality, even at the smallest pitch of 15 μm .

The final proof is in the image itself, examples of which are given in Fig. 9 for a Pelican epi-InSb FPA with an aperture of F/4.1, at temperatures of 95 K and 110 K, respectively. Even at 110 K, the image quality is very good, and only begins to degrade noticeably above 120 K.

2.4 Performance of XB_n InAsSb Bariode FPA

Except where stated otherwise, the InAs_{0.91}Sb_{0.09} *n*-type bariode structures discussed in this section were grown lattice matched to 2" or 3" GaSb substrates, in a Veeco Gen III MBE machine. The principal layers in the bariode structures were a

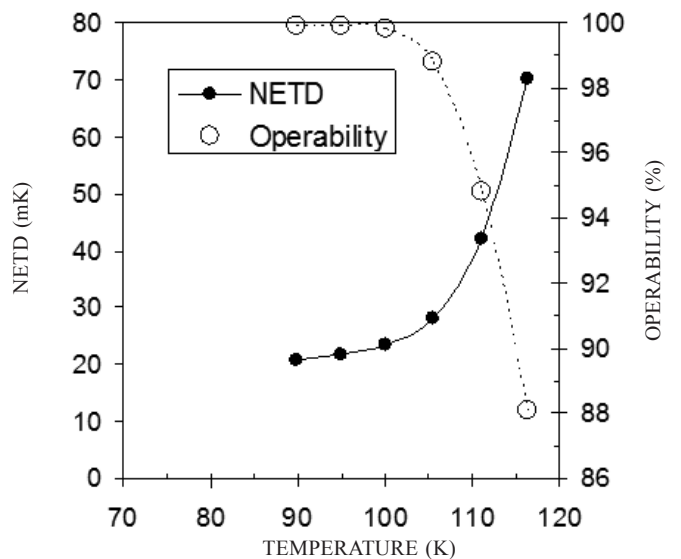


Figure 7. Temperature dependence of the NETD and the pixel operability of an epi-InSb Pelican FPA, measured with an aperture of F/4.1 in front of a Black Body at a temperature of 30 °C.

thick (1.5-3 μm) n -type $\text{InAs}_{0.91}\text{Sb}_{0.09}$ photon absorbing active layer (AL), a thin (0.2-0.35 μm) n -type $\text{AlSb}_{0.91}\text{As}_{0.09}$ barrier layer (BrL), and a thin (0.2-0.5 μm) n -type $\text{InAs}_{0.91}\text{Sb}_{0.09}$ contact layer (CL). The grown wafers were processed into 640 x 512 pixel arrays, with a 15 μm pitch. In all cases, the mesas were etched to a depth greater than the thickness of the CL, and a common contact was made to the AL outside the active device area. The arrays were flip-chip bonded with indium bumps to SCDs Pelican or Pelican-D ROICs. Pelican is the analogue version, and Pelican-D, the digital version, of SCD's 15 μm pitch ROIC. The substrate was usually etched away, and an antireflection coating (ARC) applied.

The mean dark current in our FPAs shows identical behaviour to that reported previously for single devices¹³. It can be fitted to the standard dependence for Diffusion limited behaviour of the form $J \propto T^3 \exp(-\Delta E/kT)$, yielding an activation energy of $\Delta E \sim 336$ meV. It was shown that

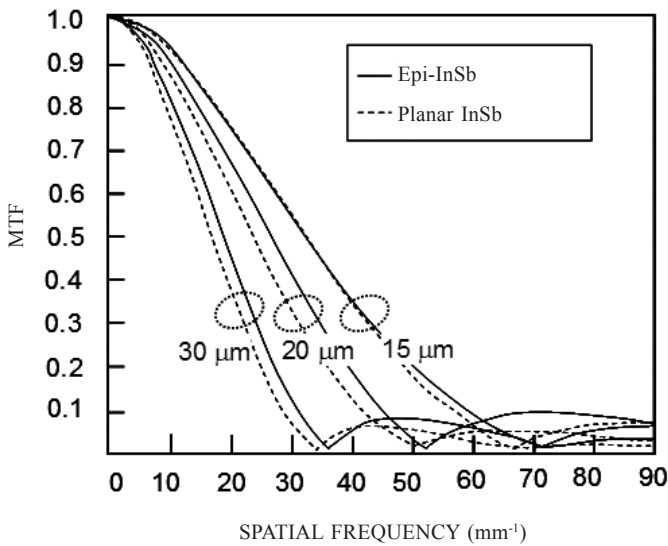


Figure 8. Modulation transfer function curves for implanted planar InSb and epi-InSb, measured on FPAs with pitches of 15 μm , 20 μm , and 30 μm .

a correction of 36 meV must be subtracted in order to take into account the dependence of the bandgap on temperature and thereby deduce the bandgap energy^{10,14,15} at 150 K. This procedure yields ΔE (150 K) ~ 300 meV, which corresponds very well to the expected bandgap energy of 302 meV (bandgap wavelength ~ 4.1 μm) for lattice matched $\text{InAs}_{1-x}\text{Sb}_x$ ¹⁵. The diffusion current can be used to deduce a value of ~ 700 ns for the minority carrier lifetime, and a value of ~ 50 μm for the bulk diffusion length^{10,14,15}. At 150 K, the typical operating dark current density is $2\text{-}3 \times 10^{-7}$ A/cm², corresponding to a pixel dark current of just a few tenths of a pico-ampere for an FPA with a 15 μm pitch. This value is demonstrated in the distribution shown in Fig. 10 for a $\text{InAs}_{0.91}\text{Sb}_{0.09}$ Pelican n -type bariode FPA at 150 K. It has a mean value of 0.2 pA and a FWHM of 15 %. This mean value is about 50 times lower than the photocurrent at F/3 for a QE of 70 % between 3 μm and 4 μm . Such a QE value is quite realistic, and will be demonstrated below. It suggests that we can achieve very good BLIP operation at 150 K, and that the detector should remain in BLIP operation at F/3 up to ~ 175 K, when the photocurrent and dark current become equal.

Figure 11 shows the temperature dependence of the NETD at F/3.2, and the pixel operability, for a 15 μm pitch Pelican D $\text{InAs}_{0.91}\text{Sb}_{0.09}$ n -type bariode FPA. The operability was determined with similar criteria to those used for the epi-InSb FPA shown in Fig. 7. The NETD and operability only begin to change above 170 K, consistent with the BLIP temperature of 175 K estimated above.

Examples of some images registered with a similar Pelican D bariode FPA to that shown in Fig. 11 are presented in Fig. 12, for an FPA operating at temperatures between 103 K and 225 K at an aperture of F/3.2. The image does not show any obvious signs of degradation until temperatures above 180 K - 190 K. These temperatures are consistent with the estimate made above for a BLIP temperature of ~ 175 K. In this detector, we have demonstrated a NETD of 17.5 mK, as shown in Fig. 13. Using a standard two point non uniformity correction and standard criteria for the identification of defective pixels, similar to those used in SCD's matured InSb detectors, the

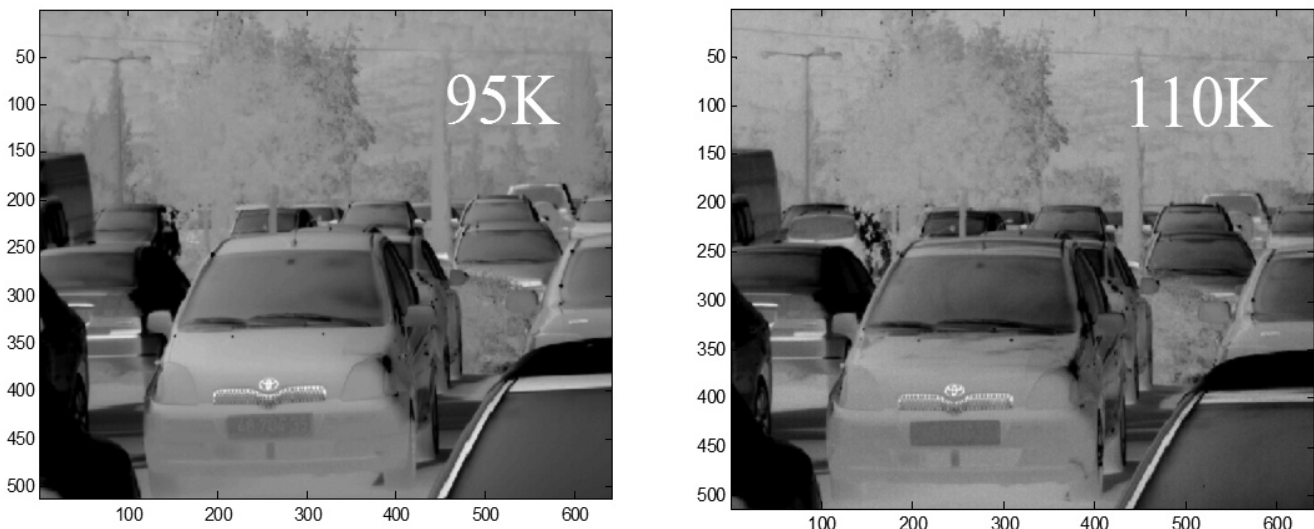


Figure 9. Images registered with a 640 x 512 15 μm pitch Pelican FPA at temperatures of 95 K and 110 K with an aperture of F/4.1.

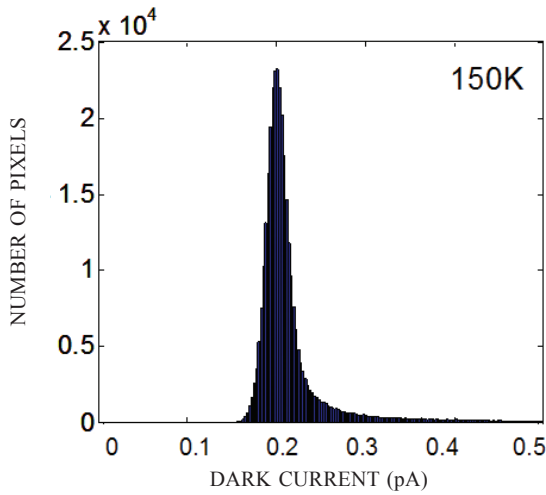


Figure 10. Dark current distribution in Pelican $\text{InAs}_{0.91}\text{Sb}_{0.09}$ n-type bariode FPA at 150 K.

pixel operability at 150 K was 99.85 %.

The mean spectral response of the bariodes of an $n\text{B}_n$ FPA bonded to SCD's Blue Fairy ROIC (30 μm pitch) was measured at 150 K. The spectrum is shown as a dotted line in Fig. 14 (a), where it is compared with the result of an optical transfer matrix simulation (solid line)¹⁴. The bariode had a 2.6 μm thick AL and an ARC with an optical thickness of 1.14 μm . The metallic contact on the top of the mesa had a low optical reflectivity, so the device was essentially a one pass device. The agreement between measured and simulated spectra is very

good when an internal quantum efficiency of 91 % is used. By increasing the reflectivity of the top contact in the simulation to ~95 %, increasing the AL thickness to 5 μm and by adjusting the thickness of the ARC for optimum performance, the upper spectrum shown in Fig. 14 (b) is obtained. The internal quantum efficiency was also increased to 95 % since the lower value fitted above is smaller than typical. Such a detector has a cut-off wavelength of ~4.15 μm at 50 % of maximum response,

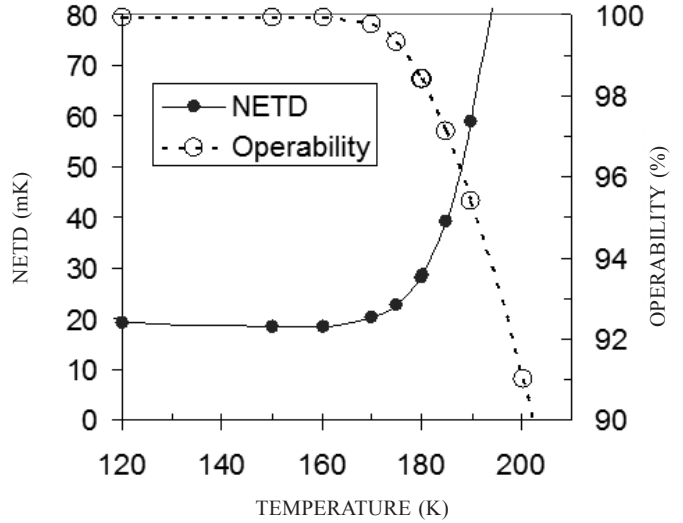


Figure 11. Temperature dependence of the NETD and the pixel operability for an InAsSb n-type Pelican-D FPA, measured with an aperture of F/3.2 in front of a black body at a temperature of 50 °C.

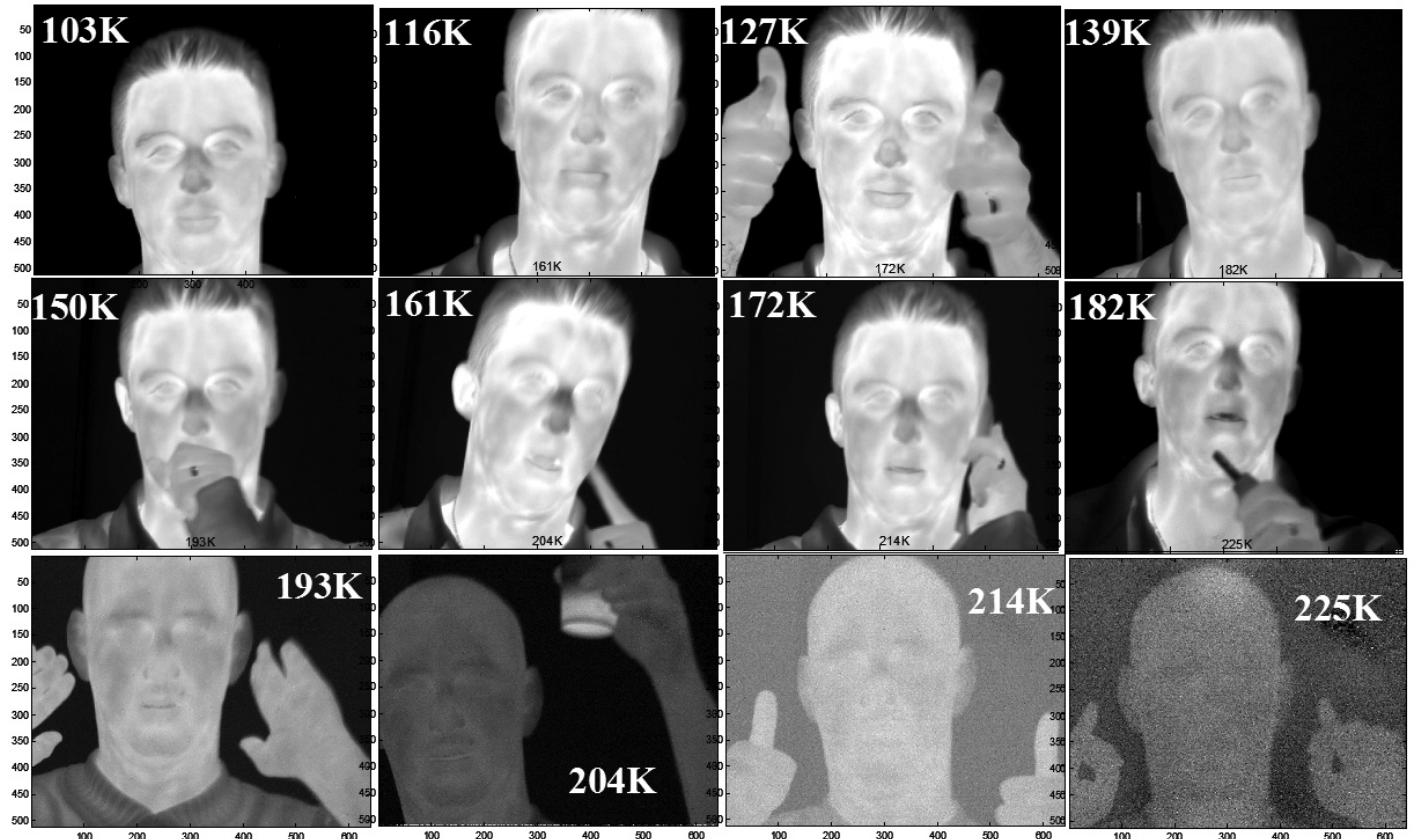


Figure 12. Images at FPA temperatures between 103 and 225K, for an n-type bariode FPA bonded to SCD's digital Pelican D signal processor. The F/number was F/3.2.

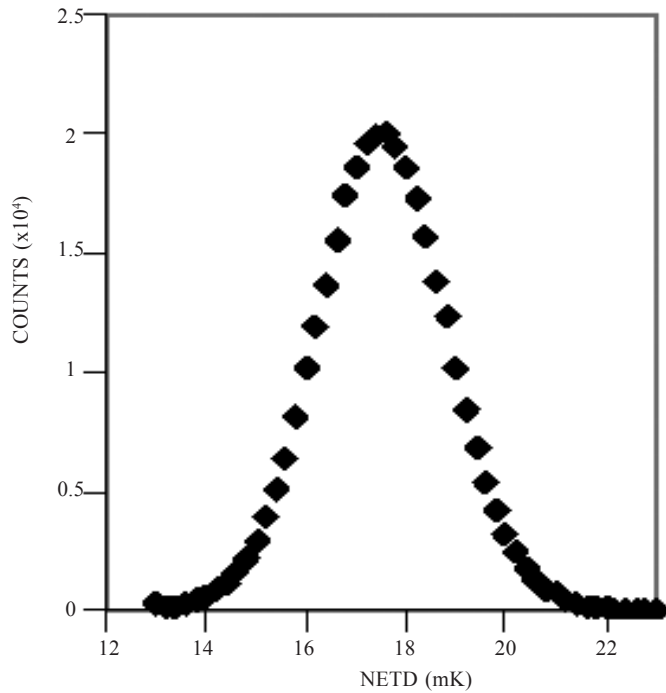


Figure 13. NETD distribution for the FPA in Figure 12 at a black body temperature of 50 °C (Peak =17.5 mK, standard deviation = 1.3 mK).

and a QE of >70 % between 3 μm and 4 μm . Fig. 14 (b) also shows how the QE and cut-off wavelength of an optimized detector increase with AL thickness.

In addition to the lattice matched $\text{InAs}_{0.91}\text{Sb}_{0.09}$ *n*-type bariode FPAs grown on GaSb substrates, discussed so far, we have also begun investigations of non-lattice matched bariodes grown on GaAs substrates¹⁶. High quality GaAs substrates can be supplied commercially at lower cost and with diameters greater than the maximum 4", currently available for GaSb. We have found that by first growing a suitable thick buffer layer we can achieve comparable performance to the lattice matched FPAs, with negligible loss of pixel operability. The lines in Fig. 15 are a 'Rule 07 Plot' due to Tennant showing the expected dark current for high performance MCT diode detectors¹. Onto this plot have been added points to indicate the typical mean dark current of our Pelican-D bariode FPAs grown on each substrate type. The FPAs were made from wafers containing nominally identical bariode structures with a 3 μm thick AL. After growth, the bandgap wavelengths of the ALs were measured optically and found to be very similar. The solid line in the Figure is that calculated using the Tennant formula¹, while the two dashed lines indicate a reasonable range of uncertainty corresponding to a factor of 2.5 increase or decrease from the Tennant value. The points showing the *n*-type bariode results fall slightly below the solid line of the Tennant formula, demonstrating that the performance of both the lattice matched and the non-lattice matched *n*-type bariode FPAs are entirely comparable with that of high quality diode FPAs made from HgCdTe with the same AL bandgap.

2.5 Summary of Results on Diodes and Bariodes

At SCD we have developed two advanced technologies for raising the operating temperature of our MWIR FPAs

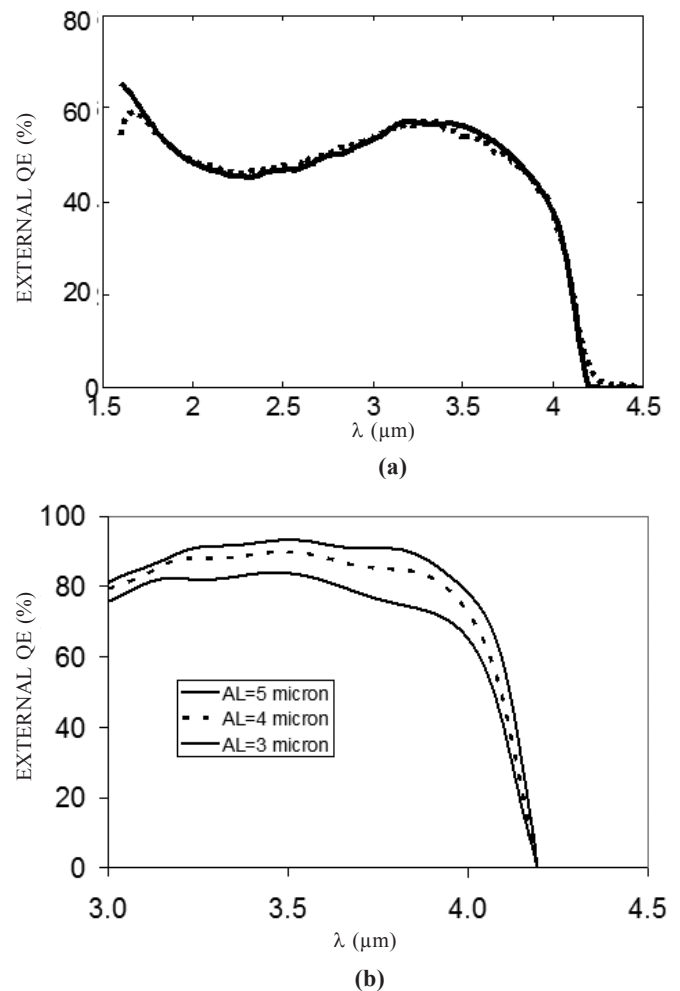


Figure 14. Optical transfer matrix simulation of QE as a function of wavelength (spectral response) at 150 K (a) for a one pass nB_n bariode detector with a 2.6 μm AL and an AR coating of optical thickness 1.14 μm (thick solid line), compared with the measured spectrum (thick dotted line) (b) for a fully optimized two pass structure with a 3 μm , 4 μm or 5 μm AL. The internal QE values used in the simulations were 91 % and 95 %, respectively.

without compromising image performance. These advanced detector arrays have pitches of 30 μm , 20 μm , or 15 μm and are compatible with SCD's analogue and digital ROICs, available in formats from 320×256 up to 1280×1024 . Both technologies are based on MBE grown $\text{InAs}_{1-x}\text{Sb}_x$ with $x=1$ or $x \sim 0.09$. These two compositions correspond to cut-off wavelengths of around 5.4 μm and 4.1 μm , respectively. We have performed a system analysis which shows that the shorter cut-off wavelength actually confers some advantages on systems designed for long range detection and identification, while for shorter ranges, the system performance is comparable in most situations. There are some applications, however, where the full MWIR window is required in any range.

In epi-InSb diodes ($x=1$), the G-R current is reduced by a factor of about 17, relative to our standard planar FPA technology. Epi-InSb FPAs operate in the temperature range 95-100K with the same cut-off wavelength and performance as

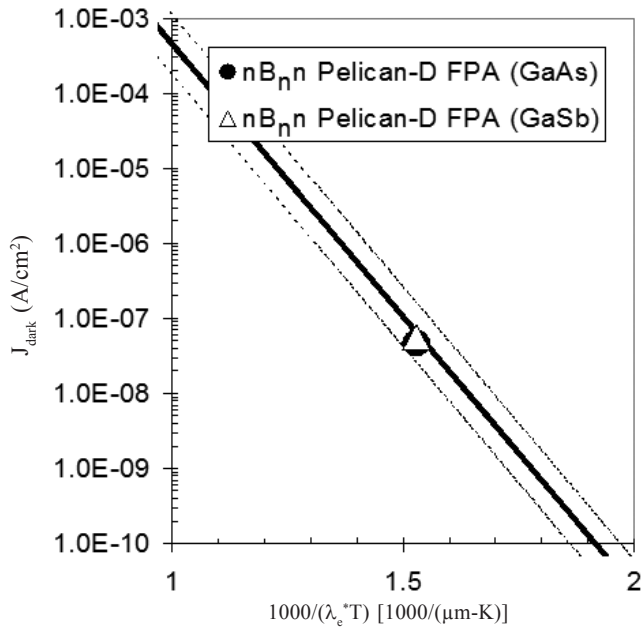


Figure 15. Dark current comparison between MCT Rule 07 and the mean value in Pelican-D $\text{InAs}_{0.91}\text{Sb}_{0.09}$ n-type bariode FPAs operating at 150 K, one of which was grown on GaSb and the other on GaAs. The AL thickness was 3.0 μm in each case.

for planar InSb. In $\text{XB}_n \text{InAs}_{0.91}\text{Sb}_{0.09}$ bariodes, the G-R current is totally suppressed and the bariode FPAs operate at 150-160 K. At F/3, they exhibit BLIP performance up to ~ 175 K.

The bariode detector arrays obey MCT Rule 07 very well and exhibit dark currents similar to the best MCT diodes with the same active layer bandgap. Moreover, they can be grown on relatively low cost 3" or 4" GaSb substrates or even larger GaAs substrates, making them a particularly attractive prospect for large scale, low SWaP, staring arrays.

Both epi-InSb and $\text{XB}_n \text{InAs}_{0.91}\text{Sb}_{0.09}$ FPAs may also be operated below their standard operating temperatures, in order to reduce the dark current to a negligible value. This is useful in applications where the incident photon flux is particularly low, or where the FPA temperature is liable to drift during operation.

3. MICROBOLOMETERS

Since the introduction of its first μ -Bolometer detector *BIRD384* in 2005, SCD has expanded the product portfolio in order to address a wide spectrum of applications. For the well established 25 μm pitch family we hold two basic formats (384 x 288 and 640 x 480) with several sensitivity grades. The tradeoff is between sensitivity and pixel time constant. Highly unstable platforms may require a relatively short time constant, whereas stable platforms can exploit the superior performance that is accompanied by longer ones. We have demonstrated successfully the use of our very high sensitivity (VHS) 25 μm pitch detector with F/2.4, for long range observation systems.

Most of the μ -Bolometer detectors are optimized to work in the LWIR band, to enable thermal imaging. For other applications such as situational awareness, we have developed the wide-band (WB) detector, where the detector absorption is optimized to both the MWIR and LWIR bands.

The 17 μm pitch family consists of a 640 x 480 (VGA) format that was introduced¹⁷ in 2010. This is the leading candidate for next generation platforms such as thermal weapon sights (TWS), driver vision enhancers (DVE) and other mid range applications. This family is currently being expanded with the high sensitivity (HS) grade and with the addition of two new formats: First, a compact 384 x 288 (QVGA) version with a minimal footprint that will address battery operated size weight and power (SWaP) sensitive applications, and a large 1024 x 768 (XGA) FPA for platforms requiring high resolution and a wide field of view (FOV). Systems based on this array have the potential to compete with older and more complex cooled 2nd generation scanning arrays, such as MCT-TDI-288x4.

The remainder of this section is organized as follows: In the first part we describe the main features and radiometric performance of three detectors: the VHS detector and its demonstrator, the WB detector and demonstrators from the 17 μm pitch family. In the last part we present *TRM3* system simulations, comparing the predicted performance of an XGA based system with state of the art 2nd generation scanning LWIR arrays. It will be shown that similar and even better recognition ranges may be achieved with the μ -Bolometer detector under various system constraints. This is partly due to the recent introduction of the high sensitivity 17 μm pixel (HS) that will be described in detail.

3.1 25 μm VHS Detector for Long Range Applications

The development of the 17 μm pixel has enabled us to optimize the process for the 25 μm technology and to improve the temporal NETD. The latest improvement was achieved by optimizing the membrane structure, enhancing the pixel fill factor at the expense of reducing the contact area and the critical dimensions of the bolometer.

Very high sensitivity (VHS) 25 μm pitch FPAs, were characterized, providing NETD < 15 mK @ F/1, for a 30 μs line integration period. The thermal time constant of the pixel is < 20 msec, which is suitable for a 30Hz frame rate system. In order to validate the mechanical integrity, several samples were packaged and then underwent the strongest thermal weapon sight (TWS) environmental tests. These tests were successfully completed and included various vibration cycles, mechanical shocks and aggressive thermal cycles.

In order to demonstrate the use of the VHS detector for long range application, we designed and integrated a single FOV, long range observation system with F/2.4, IFOV of 79 μrad and a clear aperture of 132 mm (Fig. 16 (a)). We have measured (including the lens) NETD < 70 mK with a VGA detector. The combination of an exceptionally small IFOV and low temporal system NETD enables the recognition of a human and vehicle at fairly large distances, as shown in Fig. 16 (a).

3.2 WB Detector for LWIR and MWIR

Most of the μ -Bolometer detectors are optimized to work in the LWIR band, to enable thermal imaging. For other applications such as situational awareness, we have developed the wide-band (WB) detector, where the pixel absorption

is tuned to both the MWIR and LWIR bands, as described in Fig. 17. Both detectors (WB and regular LW) have a Germanium window with AR coating. For the WB detector the window transmission between 3-14 μm is above 90 %, and for the standard detectors the window transmission between 8-14 μm is above 90 %.

The WB detector can be used as a dual band detector (MWIR and LWIR). This mode enables us to benefit from the two bands (without being able to separate the signal from the two bands), the LWIR band for thermal images of a scene at ~ 300 K, and the MWIR band for detecting specific events in this spectral range.

The WB detector can also be used as a MWIR detector, with the addition of a ‘hot’ MWIR filter, at the system level. In this mode the thermal image is relative poor, due to the lack of

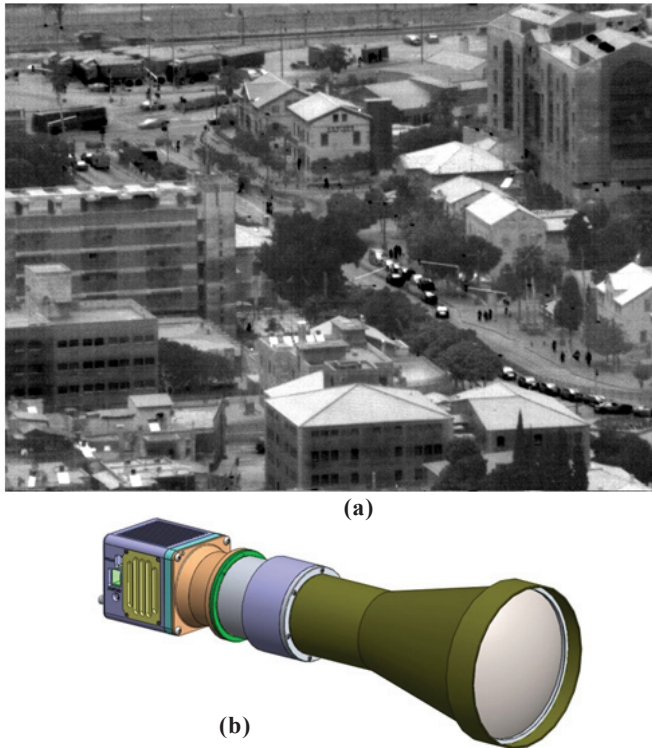


Figure 16. (a) Image from range of 2 km, (b) Schematic of the 25 μm VHS F/2.4 system demonstrator.

thermal radiation in the MWIR band from targets at 300K.

3.3 17 Micron VGA for Mid-Range Applications

The basic architecture of the ROIC was presented elsewhere¹⁸. Although it follows closely the successful framework of the previous 25 μm pitch designs, the new capabilities of the 0.18 μm CMOS process support an internal ‘coarse NUC’ (Compensation) mechanism and a more sophisticated interface management unit. This in turn considerably facilitates the user interface and was implemented in all 3 designs (QVGA, VGA, and XGA).

One of the key challenges in scaling down the pixel dimensions was to retain the high repeatability and operability of the mature 25 μm product line. The results are shown in Fig. 18 where we demonstrate the operability collected for several production batches consisting of close to 600 VGA detectors. The majority of the detectors reside above 99.9 %,

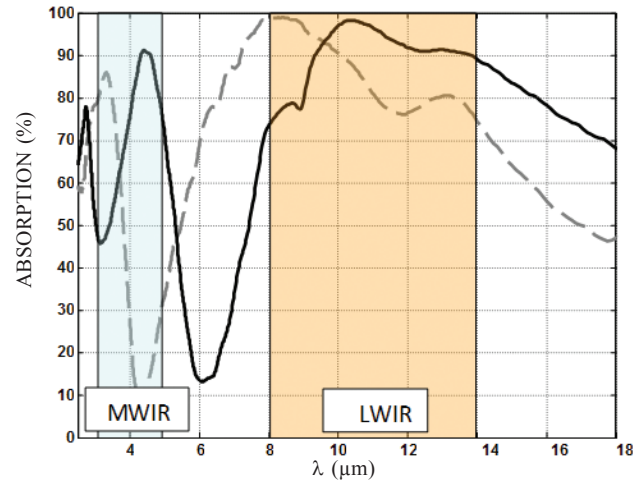


Figure 17. Pixel absorption: WB pixel (black, solid) and LW pixel (gray, dash).

which is also the typical value for our 25 μm production line¹⁹.

Another important aspect is the ability to operate the detector with the TEC-LESS or ‘Power Save’ mode²⁰. In Fig. 19 we show the variation of the NETD as a function of FPA temperature. The behavior is relatively smooth with a plateau below 40°C, the plateau continues even for lower FPA temperatures. For higher FPA temperatures there is some deterioration which is due mainly to the increased contribution of the ROIC floor noise. Still, even at 70 °C the NETD is lower than 60 mK. Since the detector was launched, it has been integrated successfully into various video engines and cameras providing state of the art performance²¹.

In the past year special effort was devoted to the improvement of the temporal NETD or SNR of the 17 μm pitch pixel. This was achieved via pixel architecture and process modifications, and the outcome is the 17 μm High Sensitive (HS) pixel. In Fig. 20 we demonstrate the temporal NETD distribution measured for F/1 optics at a frame rate of 60 Hz. The peak of the distribution is around 23 mk for the HS version and 40 mk for the standard detector version. The HS penalty is manifested in a longer time constant, but due to the relatively

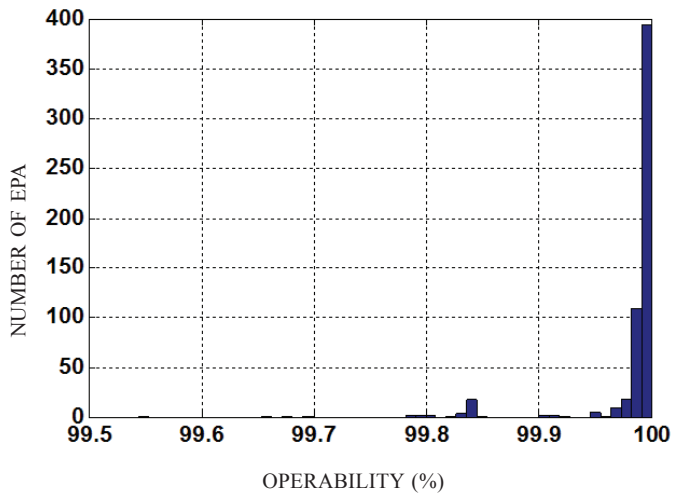


Figure 18. 17 μm VGA detector operability statistics (600 detectors).

low thermal capacitance²² it is still below 12 msec.

3.4 17 Micron QVGA for Low ‘SWaP’ Applications

In this section we describe the next product of the 17 μm family that is currently in the final stages of development. It is a compact 384 x 288 (QVGA) version with a ceramic package and minimal footprint. This detector will address the fast growing segment of low SWaP battery operated applications (e.g. goggles, miniature weapon sights, etc.).

The target specification is summarized in Table 3. The main design goals are as follows:

- Size: small package footprint (roughly 20 x 20 cm²).
- Weight < 10 gm.
- Power: TEC-LESS operation with power dissipation lower than 230 mW @ 60Hz.
- Affordable for mid-end and high volume applications

Special attention was devoted to size and weight reduction. The reduction was achieved by several means. Transformation to a ceramic package allows for a smaller pitch between the pins. We have also eliminated the need for a vacuum pipe and pumping will be done in an especially designed vacuum assembly machine. The package height was reduced as well due

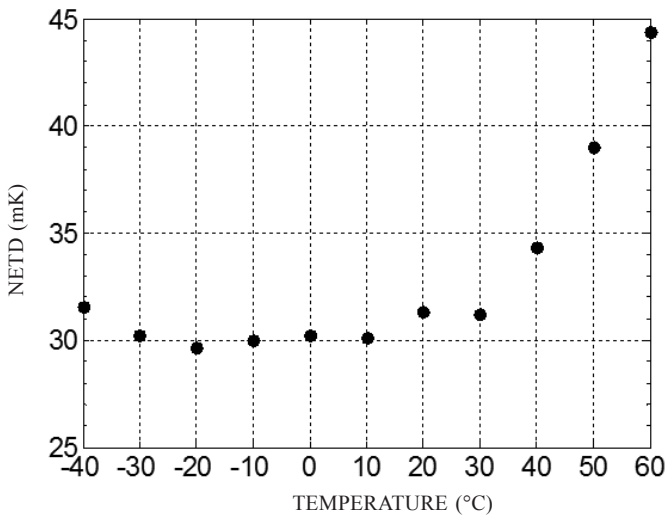
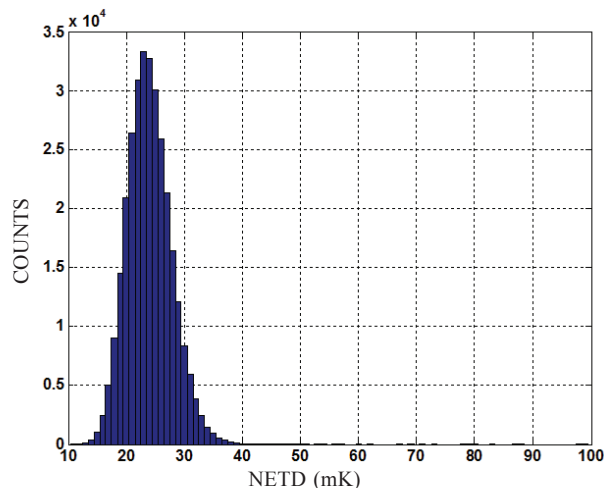


Figure 19. Median temporal NETD (F/1, 60 Hz) vs FPA temperature.



to the elimination of the TEC. The reduced weight compared with a metallic package is important for various applications. The package is shown in Fig. 21.

Based on our current, rest array characterization results we predict a temporal NETD better than 40mK @ F/1, 120 Hz. The maximum frame rate is 100 Hz (120 for 320 x 240) with a single video output, and 200 (240) Hz with 2 video lines. This is an important feature for some applications that demand high frame rates (e.g. MWS). The product will also utilize the advantages of the advanced 0.18 μm CMOS technology in terms of power and flexibility.

The ‘TEC-LESS’ performance is based on the superior uniformity of the VO_x process and the small deviation of the

Table 3. Target specification of the BIRD384/17 μm detector

Parameter	Performance
Array Size	EUR (Default): 384 × 288; USA format: 320 x 240
Temperature stabilization	Not required (TECLESS)
Sensitivity (NETD)	≤ 35 mK @ τ < 10 mSec, 25°C and f/1, 50 Hz Frame-Rate
Intra scene dynamic range	100K
Nominal frame rate	25 / 50 Hz @ EUR Format or 30/60 @ USA format
Master clock	25/50 MHz max (Varies with frame rate)
Video output	1 with 25Hz/30Hz/50Hz/60Hz/120Hz frame-rate or 2 with 200Hz / 240Hz frame-rate.
Video output voltage span	2V (0.5V÷2.7V) Nominal; Load: Max. C ≤ 20pF, R ≥ 1 MΩ
Supplies	5V analog, 1.8V digital, 3.5V video O/P
Power	P ≤ 230 mW @ 60Hz Frame-Rate, One Video output
Dimensions	20 mm x 20 mm x 6 mm
Weight	10 g (Ceramic package)
Operating temperature	-35 °C ÷ +65 °C, 25°C Nominal
Storage temperature	-46 °C + 71°C

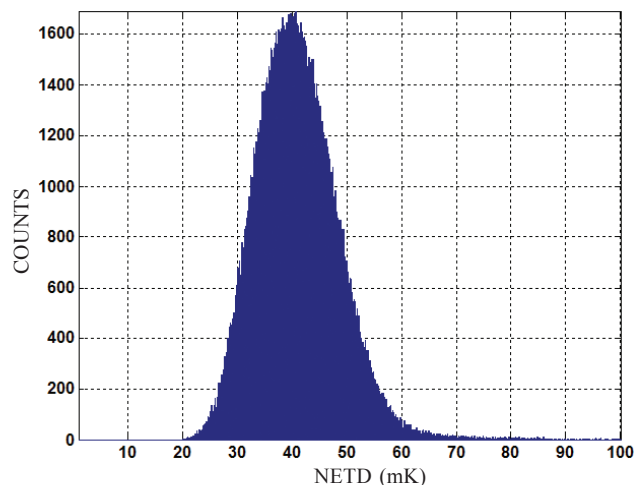


Figure 20. VGA detector measured temporal NETD (F/1, 60 Hz) of the HS version (left) and the standard version (right).

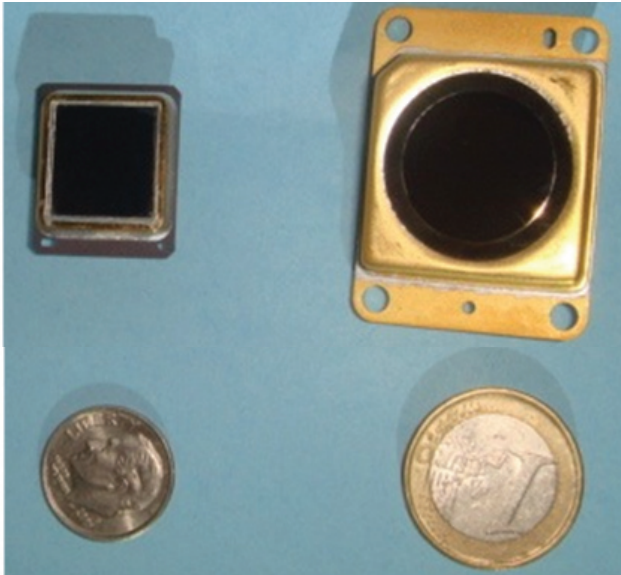


Figure 21. BIRD384/17 μm package (left), compared to BIRD640/17 μm metallic package (right).

temporal NETD with FPA temperature as depicted in Fig.19.

3.5 17 Micron XGA Detector for Long Range Sights

Long range sights or targeting systems are extremely demanding due to the combination of high spatial resolution, low temporal NETD and a wide enough field of view. For practical systems it is very difficult to support these constraints simultaneously: high resolution (small IFOV) translates into a large focal length, whereas low system NETD limits the f-number. As will be shown in the next section, if we limit the system clear aperture to a reasonable diameter (e.g. 120 mm) the f-number should be at least 1.5 and even higher in order to provide a high enough focal length and resolution. Such a high f-number is challenging for micro Bolometer technology in terms of sensitivity. For this purpose SCD is developing an XGA (1024 x 768) FPA based on the 17 μm HS pixel technology.

Table 4 summarizes the specification of this detector. It follows closely the existing ROIC architecture (including internal compensation) with the necessary adjustments that are due to the larger format. The improved pixel design (HS) supports a temporal NETD lower than 35 mK @ F/1, 30Hz which is extremely aggressive compared with current state of the art detectors²³.

One of the first samples was integrated into a demonstration camera with a 210 mm focal length and F/1.5 optics. Proprietary algorithms were employed in order to maintain the spatial noise (RNU) below the temporal noise. The image is shown in Fig. 22. The combination of an exceptionally small IFOV of 80 μRad and temporal system NETD of roughly 60 mK enables the recognition of small details at fairly large distances. The product is currently in the final stages of qualification.

3.6 System Performance Simulations

The XGA detector has the potential to replace or upgrade existing cooled LWIR scanning systems. In order to validate this assumption, we have performed TRM3 system

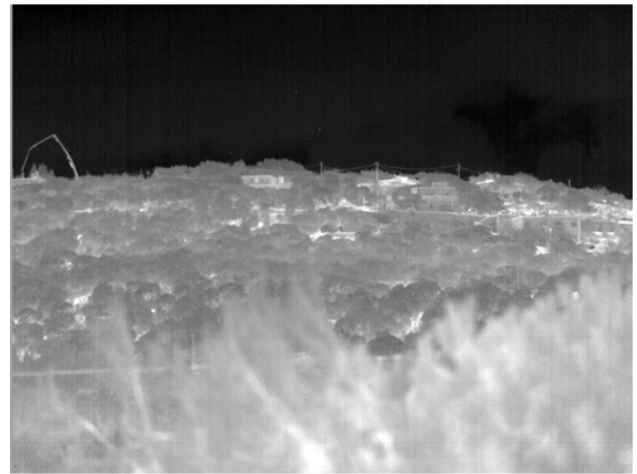


Figure 22. Captured images with a 210 mm focal length system: The houses on the ridge and the power lines are 2 km away.

Table 4. Target specification of the XGA/17 μm detector

Parameter	Performance
Array format	1024 x 768 elements
Pitch	17 μm
Readout technology	Si CMOS technology 0.18 μm
Readout functionality/Architecture	Analogue within the XGA array, Digital 14 bit output from a proximity electronics card
Spectral bandwidth	8 – 14 μm
Pixel operability	> 99.5%
Maximum frame rate	60 Hz
Thermal time constant	< 12 msec
Digital I/O	1.8 V CMOS
NETD (F/1, 30 Hz, 25 deg)	< 35 mK
FPA operating temperature	-40 °C to +65 °C
Real time compensation	Internal within the ROIC

simulations²⁴ comparing the expected performance of the uncooled XGA 17μm FPA with state of the art 288 x 4 MCT TDI scanning arrays. The requirements and system constraints are as follows:

- NATO target: 2.3 m x 2.3 m
- ΔT (Target-Background) = 2 °C
- Atmosphere extinction coefficient = 0.16 to 0.4 (variable)
- Optical aperture = 120 mm (system constraint)

Table 5 summarizes the system parameters for the XGA and typical SADAI 288 x 4 time delayed integration (TDI) cameras. Both systems are assumed to operate at a 30 Hz frame rate. For the sake of comparison we assume identical optical transmission (approximately 80 %) and display properties.

The TRM3 calculation results for the systems described in Table 5 are shown in Fig. 23. We present the target recognition range as a function of atmospheric extinction for the μ-Bolometer XGA and MCT TDI 288 x 4 array respectively.

The global RNU is assumed to be 70% of the NETD. This is a remarkable challenge for μ -Bolometer systems and requires special image processing algorithms²⁵. These simulations show that under a wide range of atmospheric conditions the XGA performs better than the TDI 288x4. The margin diminishes for poorer atmospheric conditions. The XGA detector also supports a considerably larger FOV which is extremely important for high end applications.

Another important segment is remote weapon stations where we consider human recognition. In this case the target size is 0.5 m x 1.6 m with $\Delta T = 5^\circ\text{C}$. Fig. 24 presents the calculated recognition range for a 120 mm aperture. The range is slightly above 1 km and, as expected, it is hardly affected by atmospheric conditions.

In conclusion, high-end μ -Bolometer systems hold great

Table 5. System parameters used in the TRM3 calculation

Detector parameter	2 nd Gen MCT TDI 288 X 4	Uncooled XGA
F-number	1.86	1.67
Detector Pixel	28 x 25 μm	17 x 17 μm
Focal length	225 mm	200 mm
IFOV	110 μRad	85 μRad
FOV	2.7 ^o x 2 ^o	5 ^o x 3.75 ^o
Spectral range	7.8 – 10.2 μm	8 – 14 μm

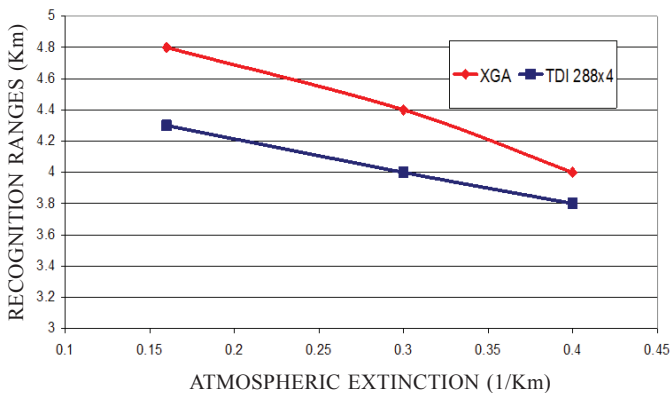


Figure 23. Calculated recognition ranges for a NATO target vs. atmospheric extinction for uncooled XGA and cooled MCT-TDI 288 x 4 based systems. (RNU= 0.7*NETD).

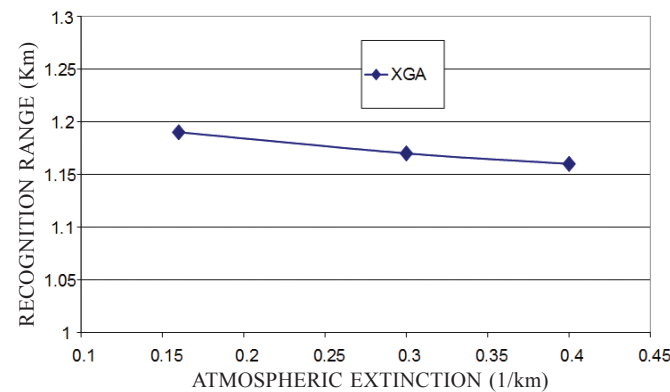


Figure 24. Calculated human recognition ranges for similar system and atmospheric conditions.

potential for replacing or upgrading 2nd generation cooled scanning systems. The introduction of μ -Bolometer technology should reduce the ‘cost of ownership’ of such systems dramatically, and as a result increase their proliferation.

3.7 Summary of Microbolometers

We have presented an overview of SCD’s state of the art microbolometer VO_x uncooled detector arrays.

The VGA 25 μm pitch VHS detector and the F/2.4 demonstrator, exhibit performance comparable with traditional second generation cooled LWIR detectors. The WB detector is ideal for applications such as situational awareness, where MWIR signal detection is important.

Three new detectors cover a wide range of applications: 17 μm VGA for mid-range TWS and hand held systems, 17 μm QVGA for low SWaP applications, and 17 μm XGA format for long-range large FOV sights.

TRM3 simulations have been performed in order to compare the expected system performance of an XGA microbolometer detector with 2nd generation scanning MCT LWIR 288 x 4 TDI arrays. The calculations show that similar recognition ranges may be achieved under various system constraints.

4. CONCLUSIONS

High end detector arrays at SCD with low NETD at medium and large F/numbers are based on InSb diodes ($\lambda_c = 5.4 \mu\text{m}$) and XB_n InAsSb bariodes ($\lambda_c = 4.1 \mu\text{m}$). Epi-InSb diodes have a reduced G-R dark current while in the patented XB_n architecture the G-R dark current is totally suppressed. By reducing the dark current, the operating temperature of the detector can be raised, leading to significant reductions in the SWaP figure of the complete IDCA. In epi InSb operating at 95 K, the required cooling power is reduced by about 20 % and this reduction increases to 60 % for InAs_{0.91}Sb_{0.09} bariode detectors which operate at 150 K. The result is an improved range of solutions for a wide range of applications, including faster cool-down time and mission readiness, lower cooling power, higher cooler reliability, and more compact detectors for volume-critical applications. Pelican or Pelican D, 15 μm pitch, epi-InSb FPAs are now in production at SCD. 15 μm pitch XB_n InAs_{0.91}Sb_{0.09} bariode FPAs will be in production from the second quarter of 2013.

Microbolometer detectors operate with low NETD at room temperature, with small or medium F/numbers. A VGA 25 μm pitch VHS detector exhibits performance at F/2.4 comparable with traditional second generation cooled LWIR detectors. The WB detector is ideal for applications such as situation awareness, where MWIR signal detection is important. Three new detectors cover a wide range of applications: 17 μm VGA for mid-range TWS and hand held systems, 17 μm QVGA for low SWaP applications, and 17 μm XGA format for long-range large FOV sights.

Using TRM3 simulations we have shown that in many applications the shorter cut-off wavelength of the XB_n detector is not a disadvantage because the reduction in photon flux is compensated by the higher transmission of the atmosphere in the ‘blue’ MWIR window. Thus similar detection and

recognition ranges are found in both InSb diode arrays and InAsSb bariode arrays under a wide range of conditions. Similarly we have shown that uncooled microbolometer arrays can exhibit similar recognition ranges to those of cooled 2nd generation MCT LWIR 288 x 4 TDI arrays. Hence, XB_n arrays can perform many of the roles traditionally performed by InSb arrays, and high-end microbolometer systems have the potential for upgrading 2nd generation scanning systems, in each case, with many cost and reliability related benefits of a smaller, lighter and lower power system.

ACKNOWLEDGEMENTS

We would like to acknowledge support for this work received from the Israeli Ministry of Trade and Industry (MOITAL) and Israeli Ministry of Defense (IMoD). The authors are also indebted to numerous engineers and technicians for their dedicated contribution to the development and production of the detectors.

REFERENCES

- Tennant, W.E. 'Rule 07' revisited: still a good heuristic predictor for p/n HgCdTe photodiode performance? *J. Electron. Mater.*, 2010, **39**, 1030.
- Glozman, A.; Harush, E.; Jacobsohn, Eli; Klin, O.; Klipstein, P.C.; Markovitz, T.; Nahum, V.; Saguy, E.; Oiknine-Schlesinger, J.; Shtrichman, I.; Yassen, M.; Yofis, B. & Weiss, E. High performance InAsSb MWIR detectors operating at 100 K and beyond. Proc. SPIE, 2006, **6206-0M**.
- Shockley, W. & Read, W.T. Statistics of the recombinations of holes and electrons. *Phys. Rev.* 1952, **87**, 835.
- Hall, R. N. Electron hole recombination in germanium. *Phys. Rev.* 1952, **87**, 387.
- Reago, Donald A. Future Army applications for IR focal plane arrays. <http://spie.org/x20227.xml>, 2008.
- Klipstein, P.C. Depletionless photodiode with suppressed dark current. US Patent 7,795,640 (2 July 2003).
- Klipstein, P.C. Unipolar semiconductor photodetector with Suppressed dark current. US Patent 8,004,012 (6 April 2006).
- Klipstein, P.C. XB_n barrier photodetectors for high sensitivity and high operating temperature infrared sensors. Proc. SPIE, 2008, **6940-2U**.
- Klipstein, P.C.; Aronov, D.; Berkowicz, E.; Fraenkel, R.; Glozman, A.; Grossman, S.; Klin, O.; Lukomsky, I.; Shtrichman, I.; Snapi, N.; Yassen, M. & Weiss, E. New 'bariodes' device reduces cooling requirements of infrared detectors. SPIE Newsroom 10.1117/2.120110.00319 (November 2011).
- Klipstein, P.C.; Klin, O.; Grossman, S.; Snapi, N.; Lukomsky, I.; Yassen, M.; Aronov, D.; Berkowicz, E.; Glozman, A.; Fishman, T.; Magen, O.; Shtrichman, I. & Weiss, E. XB_n barrier photodetectors based on InAsSb with high operating temperatures. *J. Opt. Eng.*, 2011, **50**, 061002
- L. Shkedy, O. Amir, Z. Calahorra, J. Oiknine-Schlesinger and Szafranek, I. Temporal dependence of spatial noise in InSb focal plane arrays. Proc. SPIE, 2000, 4028, pp.481.
- Shtrichman, I.; Fishman, T.; Mizrahi, U.; Nahum, V.; Calahorra, Z. & Aron, Y. Spatial resolution of SCD's InSb 2D detector arrays. Proc. SPIE, 2007, 6542-3M.
- Klipstein, P.C.; Klin, O.; Grossman, S.; Snapi, N.; Lukomsky, I.; Yassen, M.; Aronov, D.; Berkowicz, E.; Glozman, A.; Magen, O.; Shtrichman, I.; Frenkel, R. & Weiss, E. High operating temperature XB_n-InAsSb bariodes detectors., Proc. SPIE, 2012, **8268-0U**.
- Klipstein, P.C.; Klin, O.; Grossman, S.; Snapi, N.; Yaakobovitz, B.; Brumer, M.; Lukomsky, I.; Aronov, D.; Yassen, M.; Yofis, B.; Glozman, A.; Fishman, T.; Berkowicz, E.; Magen, O.; Shtrichman, I. & Weiss, E. XB_n barrier detectors for high operating temperature. Proc. SPIE, 2010, **7608-1V**.
- Klipstein, P.C.; Klin, O.; Grossman, S.; Snapi, N.; Yaakobovitz, B.; Brumer, M.; Lukomsky, I.; Aronov, D.; Yassen, M.; Yofis, B.; Glozman, A.; Fishman, T.; Berkowicz, E.; Magen, O.; Shtrichman, I. & Weiss, E. MWIR InAsSb XB_n detectors for high operating temperatures. SPIE, 2010, **7660-2Y**.
- Weiss, E.; Klin, O.; Grossmann, S.; Snapi, N.; Lukomsky, I.; Aronov, D.; Yassen, M.; Berkowicz, E.; Glozman, A.; Klipstein, P.C.; Fraenkel, A. & Shtrichman, I. InAsSb-based XB_n bariodes grown by molecular beam epitaxy on GaAs. *J. Cryst. Growth*, 2012, **339**, 31.
- Mizrahi, U. New developments in SCD's 17 μm VOx μ-Bolometer product line. Proc. SPIE 2010, **7660**.
- Fraenkel, A. SCD's Uncooled detectors and video Engines for a wide range of applications. Proc. SPIE, 2011, **8012-04**.
- Mizrahi, U. Large format and high sensitivity VOx μ-Bolometer detectors at SCD. Proc. SPIE, 2007, **6542**.
- Fraenkel, A. Advanced features of SCD's Uncooled detectors. *Opto-Electronics Review*, 2005, **14**, 47.
- Schapiro, F. Modular, open architecture Uncooled video engines based on OMAPTM 3530 DSP. Proc. SPIE, 2011, **8012-1D**.
- Fraenkel, A. BIRD640: SCD's high sensitivity VGA VOx μ-Bolometer detector. Proc. SPIE 2007, **6737**, 6737-0U.
- Schapiro, F. SCD cooled and uncooled detectors roadmap. OPTRO 2010 Conference, Paris, February 2010.
- Wittenstein, W. Thermal range model TRM3, infrared technology and applications XXIV. Proc. SPIE, 1998, **3436**, pp. 413-424.
- Mizrahi, U. New features and development directions in SCD's μ-Bolometer technology. Proc. SPIE, 2008, **6940**, 6940-20.

CONTRIBUTORS

Dr Philip Klipstein received his BA and PhD in Physics from Oxford University and Cambridge University, respectively. After two years as a Junior Research Fellow at Cambridge, he moved to a tenured post at Imperial College, London. Research included transport and optics in GaAs/AlAs and Si/Ge. In 1990, he returned to Oxford University, adding research into antimonide heterostructures. He joined Semiconductor Devices (SCD) in 2000. He has published more than 120 research papers.

Dr Udi Mizrahi received his MSc and PhD in Physics, from the Technion, Israel Institute of Technology, in 1999 and 2004, respectively. During his PhD he conducted research on 'Time Resolved Correlation Spectroscopy of Single Photons from Semiconductor Quantum Dots'. He joined Semiconductor Devices (SCD) in 2004.

Dr Avraham Rami Fraenkel received his MSc and DSc in Electrical Engineering from the Technion, Israel Institute of Technology, in 1986 and 1993, respectively. Presently working at Semiconductor Devices (SCD). Earlier he worked as project manager for CyOptics, specializing in 40 GHz optical communication components.

Dr Itay Shtrichman, received his MSc and PhD in physics from the Technion, Israel Institute of Technology, in 1995 and 1999, respectively. His research was focused on the dynamics of carriers in semiconductor quantum structures. He spent two years as a post-doctoral researcher at the University of California, Santa Barbara. He joined SCD in 2003. He has published more than 30 refereed and conference papers.